







Direct Measurements of Activation Energies for Surface Diffusion of CO and CO₂ on Amorphous Solid Water Using In Situ Transmission Electron Microscopy

Akira Kouchi¹, Kenji Furuya² , Tetsuya Hama^{1,4} , Takeshi Chigai¹, Takashi Kozasa³ , and Naoki Watanabe¹ ¹ Institute of Low Temperature Science, Hokkaido University, Sapporo, Hokkaido 060-0819, Japan; kouchi@lowtem.hokudai.ac.jp² Center for Computational Sciences, University of Tsukuba, 1-1-1 Tennoudai, Tsukuba 305-8577, Japan³ Department of Earth and Planetary Sciences, Hokkaido University, Sapporo, Hokkaido 060-0810, Japan

Received 2019 December 22; revised 2020 February 18; accepted 2020 February 19; published 2020 March 4

Abstract

The importance of the activation energy of surface diffusion (E_{sd}) of adsorbed molecules on amorphous solid water (ASW) has been widely discussed in terms of chemical reactions on ASW at low temperatures. However, in previous work, E_{sd} has not been measured directly but estimated from indirect experiments. It has been assumed in chemical network calculations that E_{sd} is between 0.3 and 0.8 of the desorption energies of a molecule. It remains important to obtain direct measurements of E_{sd} . We performed in situ observations of the deposition process of CO and CO₂ on ASW using transmission electron microscopy (TEM) and deduced the E_{sd} of CO and CO₂ on ASW to be 350 ± 50 and 1500 ± 100 K, respectively. The value of E_{sd} of CO is approximately 0.3 of the total adsorption energy of CO on ASW, i.e., much smaller than assumed in chemical network calculations, where the corresponding figure is 575 K, assuming approximately 0.5 of the desorption energy. We demonstrated that TEM is very useful not only for the observation of ices but also for the measurement of some physical properties that are relevant in astrochemistry and astrophysics. Using the E_{sd} of CO measured in the present study (350 K), we have updated the chemical network model of Furuya et al., confirming that CO₂ could be efficiently formed by the reaction $\text{CO} + \text{OH} \rightarrow \text{CO}_2 + \text{H}$ in the initial stages of the evolution of molecular clouds.

Unified Astronomy Thesaurus concepts: [Astrochemistry \(75\)](#); [Reaction rates \(2081\)](#); [Experimental techniques \(2078\)](#); [Ice formation \(2092\)](#); [Theoretical models \(2107\)](#); [Laboratory astrophysics \(2004\)](#); [Interdisciplinary astronomy \(804\)](#); [Interstellar molecules \(849\)](#); [Dense interstellar clouds \(371\)](#)

1. Introduction

In molecular clouds and dense cores where star formation occurs, the most abundant molecules, such as H₂O, CO₂ and CH₃OH, are present mainly on grain surfaces, including ice. These molecules are formed by two-body reactions on surfaces through the Langmuir–Hinshelwood mechanism (e.g., Watanabe & Kouchi 2002; Hama & Watanabe 2013). One of the most important parameters for determining the rates of surface two-body reactions is the activation energy of the surface diffusion of adsorbed species, but this is poorly quantified. It is, therefore, usually assumed that the activation energy of the surface diffusion of a molecule is 0.3–0.8 of the desorption energies of that molecule (Iqbal et al. 2018).

Some experimental attempts have been made to clarify the surface diffusion of CO and CO₂. Öberg et al. (2009) conducted segregation experiments using mixed ices, H₂O:CO, and H₂O:CO₂, and obtained activation energies of surface-segregation. Mispelaer et al. (2013), Karssemeijer et al. (2014), Lauck et al. (2015), and He et al. (2018) measured the diffusion of CO in amorphous solid water (ASW). In these studies, it was assumed that diffusion of CO or CO₂ occurs at the surface of pores and/or cracks in ASW and that the measured activation energies were not due to bulk diffusion but due to surface diffusion. He et al. (2017)

conducted annealing experiments of CO₂ deposited on the surface of ASW and obtained the activation energy of surface diffusion for CO₂ on ASW. Because all of the studies referred above (Öberg et al. 2009; Mispelaer et al. 2013; Karssemeijer et al. 2014; Lauck et al. 2015; He et al. 2017, 2018) used infrared spectroscopy to observe change of composition, models (e.g., rate equations) are required in order to estimate diffusion coefficients or activation energies of surface diffusion. It is thus concluded that all values obtained in these studies are model dependent.

In theoretical works, Karssemeijer et al. (2014) obtained activation energies of surface diffusion of CO on ASW, finding that the CO mobility is highly dependent on the morphology of ASW. Because the values obtained are very widely distributed (48–114 meV or 557–1320 K) and because the maximum value of 114 meV is larger than the activation energy of adsorption (Collings et al. 2003), using their results in chemical network calculations is difficult. It is, therefore, necessary to perform direct measurements of the surface diffusion coefficient of CO or CO₂ on ASW or activation energy for surface diffusion.

To overcome some of the difficulties experienced in past studies, direct observations using a transmission electron microscope (TEM) are highly valuable. Although some observations of pure H₂O ice using TEM have been performed, the primary focus of these observations included the structures formed (e.g., Honjo et al. 1956; Vertsner & Zhdanov 1966), the structural transition between high-density ASW and low-density ASW (e.g., Heide 1984; Jenniskens & Blake 1994), and the crystallization of ASW to form ice (e.g., Jenniskens & Blake 1996). Further, there have been no observations of CO and CO₂ using TEM.

⁴ Current address: Komaba Institute for Science, The University of Tokyo, 3-8-1 Komaba, Meguro, Tokyo 153-8902, Japan.



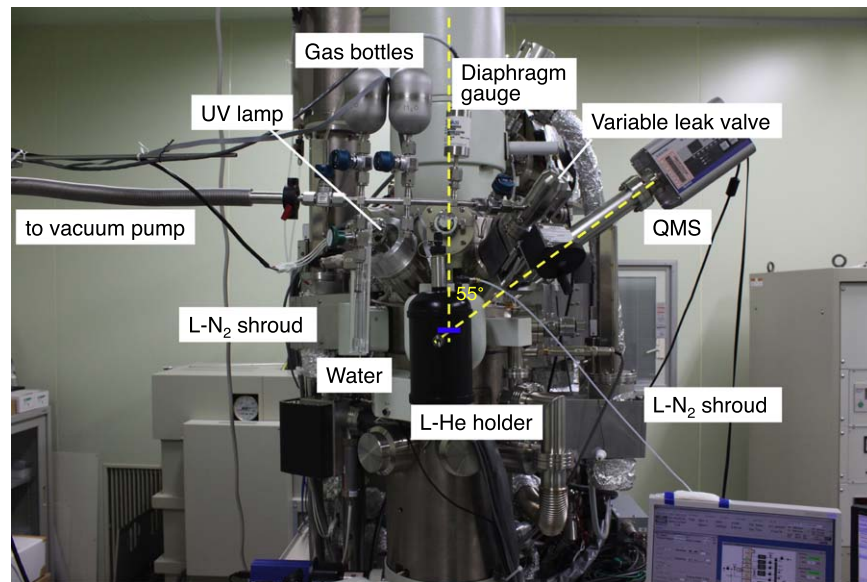


Figure 1. Newly developed UHV-TEM. Three ports are directed at the sample surface (the short blue bar) with an incident angle of 55° ; these ports are used for an ultraviolet (UV) lamp, a variable leak valve connected to a Ti tube for gas deposition, and a quadrupole mass spectrometer.

In the present study, we have performed in situ observations of the deposition process of CO and CO₂ on ASW using an ultrahigh-vacuum transmission electron microscope (UHV-TEM) and obtained the activation energies for surface diffusion of CO and CO₂ on ASW.

2. Experiment

We used a UHV-TEM (JEOL JEM-2100VL) for in situ observation of ices (Kouchi et al. 2016; Tachibana et al. 2017). A column of the UHV-TEM was evacuated using five ion pumps and two Ti sublimation pumps. The pressure between the specimen chamber and the ion pump was set at 1×10^{-6} Pa. The pressure near the specimen might be lower than 1×10^{-6} Pa as the specimen is surrounded by a liquid nitrogen shroud.

We used a liquid He cooling holder (Gatan ULTST) for sample cooling (Figure 1). A non-porous amorphous Si film with a thickness of 5 nm (SiMPore Inc. US100-A05Q33) was used as the substrate for sample deposition. We observed the Si film using high-resolution field emission TEM (JEM-2100F), and observed no pores or cracks. We also used a 0.4 mm inner diameter Ti gas inlet tube for sample deposition, which was directed at the specimen surface with an incident angle of 55° (Figure 1).

First, a ~ 10 nm thick layer of ASW was deposited at ~ 10 K. We measured the thickness of the ice samples as follows. First, a thick ice sample (e.g., 200–300 nm) was deposited at a constant deposition rate. Then, we observed the sample via TEM. By adjusting the foci at the bottom and the surface sides of the ice sample, we could measure the thickness of ices. We also measured the pressure of a gas reservoir prior and subsequent to the ice deposition. From these measurements, we obtained the relationship between the amount of deposited gas and the ice thickness. The use of thin ASW (10 nm thick) has an advantage that the contrast of the newly deposited CO or CO₂ on ASW is stronger than that of ASW.

ASW deposited at low temperatures is very porous (e.g., Stevenson et al. 1999); thus, we termed it porous ASW (p-ASW). We used the p-ASW without annealing for CO deposition. For

CO₂ deposition, p-ASW deposited at approximately 10 K was annealed at 70 K. Then, CO or CO₂ was deposited onto ASW with a deposition rate of ~ 1 nm minute⁻¹. We confirmed that crystalline CO (α -CO) was formed when deposition rate is larger than this value as stated by Kouchi (1990). We observed the entire deposition process using UHV-TEM. To avoid electron beam damage to the samples, a low dose (Tachibana et al. 2017) was applied, using an 80 kV accelerating voltage, very weak electron beam intensity ($\sim 2 \times 10^{-3}$ electrons \AA^{-2} at the sample position), and low-magnification observation ($\times 25,000$) using a CCD camera (Gatan ES500W). It is usually assumed that most 80 kV electrons will not interact with 10 nm thick ASW, implying that the ASW will not be damaged by an electron beam.

3. Results and Discussion

Figures 2(a) and (b) show the temperature dependence of the deposition processes of CO and CO₂ on ASW, respectively. It is noted that TEM observation was made during the gas deposition in situ. Electron diffraction patterns show that crystalline CO (α -CO) and CO₂ (CO₂ I) were formed at temperatures higher than 18 and 50 K, respectively. At lower temperatures (broken lines in Figure 2), amorphous CO (a-CO) and amorphous CO₂ (a-CO₂) were formed. These transition temperatures depend on the rate of deposition and are not determined uniquely (Kouchi et al. 1994), differing from the crystallization temperatures of a-CO and a-CO₂ (Watanabe & Kouchi 2008). TEM images clearly show that crystals did not grow as a uniform film but as three-dimensional islands, sometimes referred to as the Volmer–Weber growth mode. With decreasing substrate temperature, the number of crystals increased, and crystalline sizes decreased. In the case of a-CO and a-CO₂, on the other hand, uniform films were formed.

Figure 3 shows the change in the number densities of the CO and CO₂ crystals as measured via visual counting. It is clear that the number densities increased suddenly after certain incubation times, reaching saturated values. The heterogeneous nucleation rate, J , is given by the following equation (Hirth & Pound 1963,

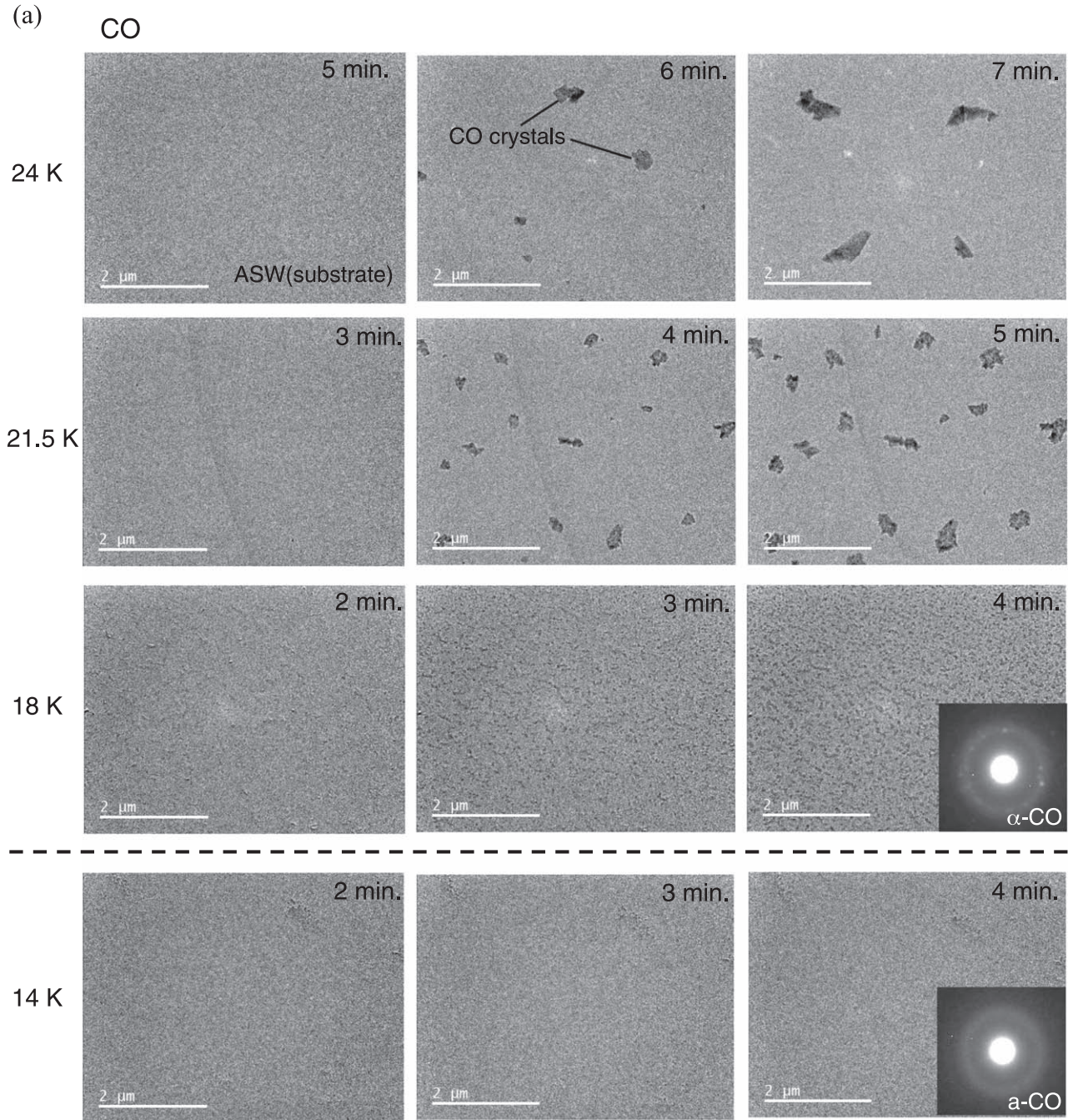


Figure 2. In situ TEM observation of the deposition of CO (a) and CO₂ (b) on ASW. The corresponding electron diffraction patterns are shown for some TEM images. In general, the contrast of TEM images increases from bright (gray) to dark (black) with the increasing atomic numbers (scattering contrast). The contrast of crystal samples is much stronger (darker) than that of amorphous sample owing to the diffraction contrast. Therefore, the detection of CO or CO₂ crystals on ASW is easier than that of a-CO or a-CO₂ on ASW. At temperatures higher than the critical temperatures shown by broken lines, crystalline CO (α-CO) and CO₂ (CO₂ I) were formed. At temperatures lower than the critical temperature, on the other hand, amorphous CO and CO₂ were deposited. White blurred images recorded in some TEM photographs are residual images in the charge-coupled device (CCD) detector.

Chapter C):

$$J = Z\omega \exp(-\Delta G^*/k_B T), \quad (1)$$

where Z is the non-equilibrium factor, ΔG^* is the free energy for the formation of the critical nucleus, k_B is the Boltzmann constant, and $\omega = n 2\pi r^* a \sin\theta$, where n is the number of adsorbed molecules, r^* is the radius of the critical nucleus, a is the diffusion jump distance, and θ is the contact angle between the substrate and the nucleus. Because the incubation time for

nucleation, τ , is defined as $\tau = 1/J$, τ is proportional to ΔG^* and q^{-1} . Therefore, the fact that the τ value of the CO₂ crystals (less than 2 minutes) was shorter than that of the CO crystals (2–6 minutes) indicates that the ΔG^* of CO₂ is lower than that of CO and/or that the θ of CO₂ is smaller than that of CO (Figure 3). The thicknesses of the CO crystals at 21.5 and 24 K in Figure 2 are larger than those of CO₂ at 55 K and 60 K, respectively; therefore, the θ value of CO₂ is smaller than that of CO, suggesting the latter possibility. In the case of CO, τ

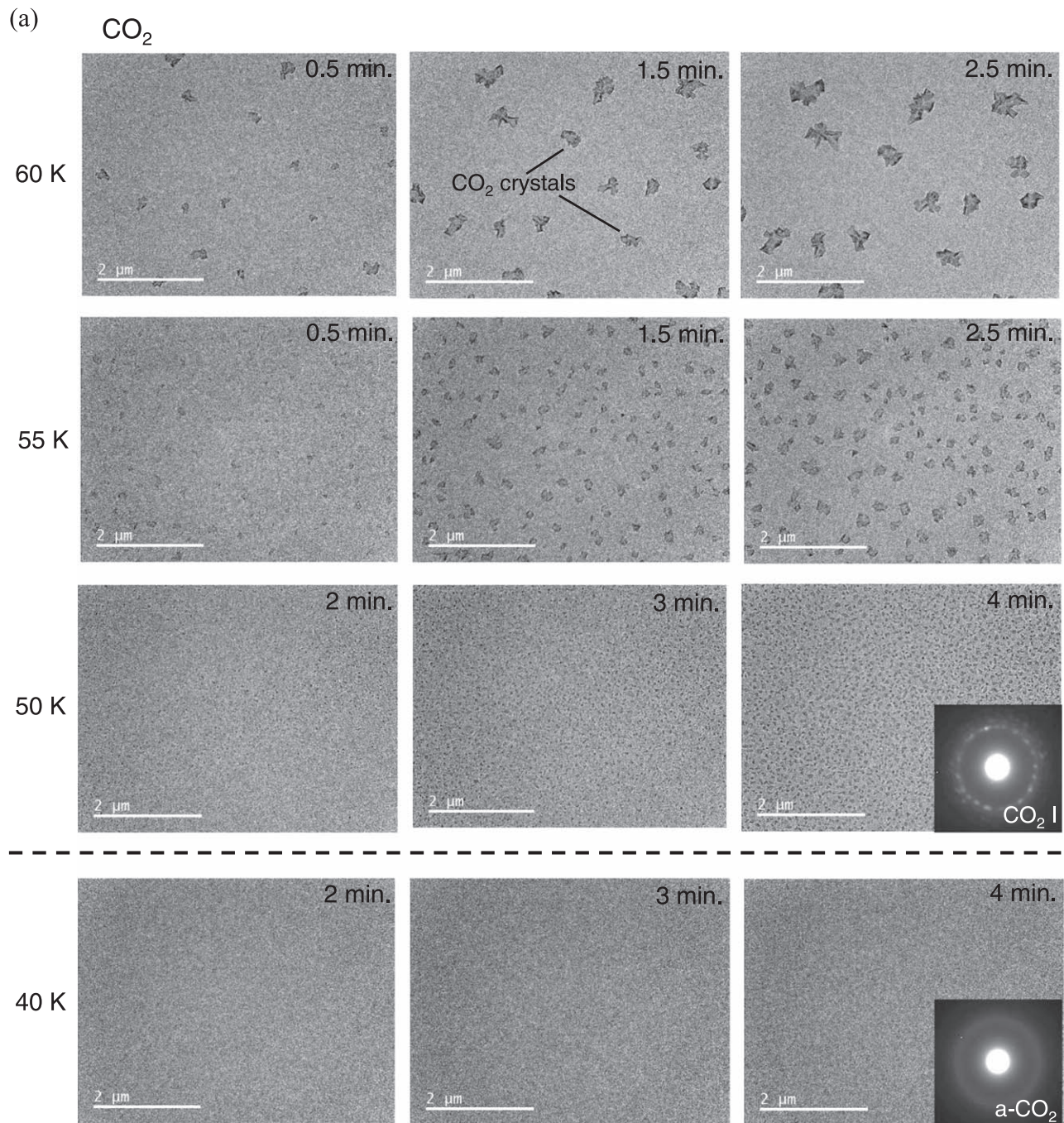


Figure 2. (Continued.)

clearly decreases with decreasing temperature. Conversely, in the case of CO_2 , such a temperature dependence has not been observed. This is likely because nucleation is the stochastic phenomenon and the observed temperature range defined by $1/T$ of CO is wider than that of CO_2 (see Figure 4).

When the nucleation ceases, the growth of crystalline islands is limited by the surface diffusion of monomers, not by that of dimers or trimers (clusters). This is verified by the following reasons. (1) At a constant incident flux and temperature, the nucleation rate should decrease with the increasing the number of crystalline islands that are larger than the critical size,

because the growth of islands via the diffusion of monomers should be the dominant process rather than the nucleation. (2) During the growth stage of stable crystalline islands, growth via cluster-cluster collision can be ignored compared with that via the attachment of monomers. In this case, we were able to obtain information on surface diffusion from the distance between islands. From the saturated number densities, N_s , mean distances between crystalline islands, L , were derived using the relation $L = (\pi N_s)^{-1/2}$. The mean diffusion distance, X , of CO or CO_2 on ASW is defined to be half of L . According to Smith (1995) (Chapter 5.2), when desorption of molecules is ignored,

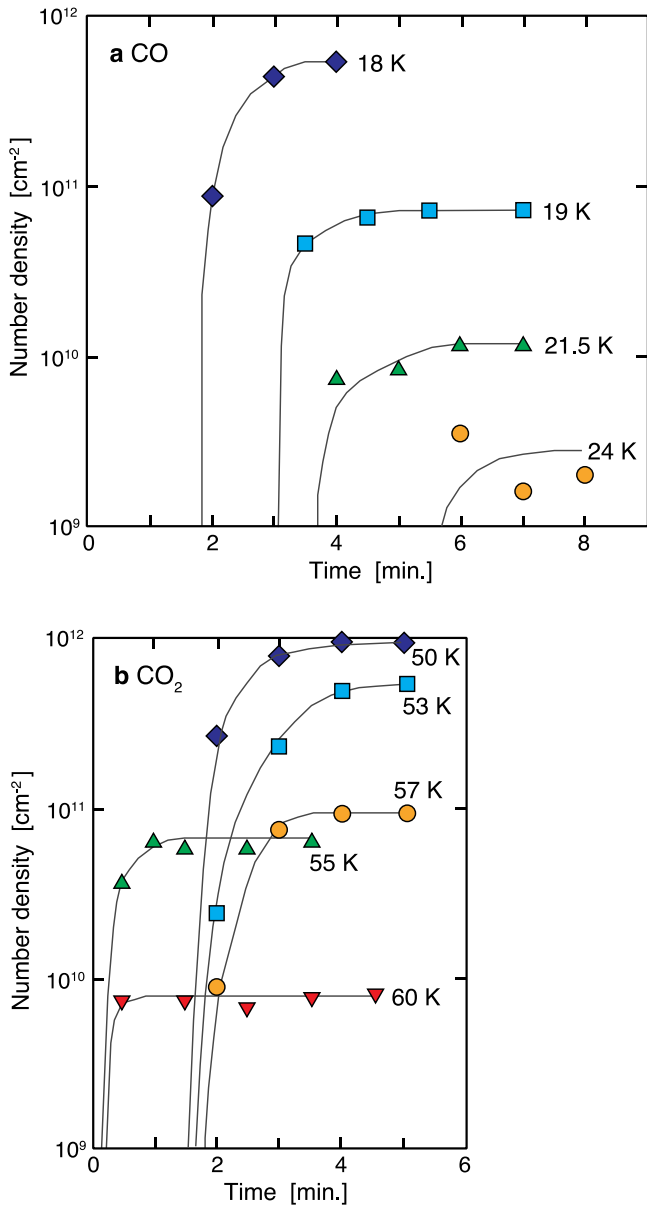


Figure 3. Number densities of CO (a) and CO₂ (b) crystals vs. deposition times for various substrate temperatures. The lines are guides for the eye.

X is expressed by

$$X = a(\nu n_0/F)^{1/2} \exp(-E_{sd}/2RT), \quad (2)$$

where a is hop distance, ν is the frequency factor, n_0 the number of adsorption sites, F the deposition flux, E_{sd} the activation energy of surface diffusion, R the gas constant, and T is the temperature. The above assumption that the desorption of molecules could be ignored is supported because a sticking coefficient of CO₂ onto non-porous ASW (np-ASW) is unity at temperatures lower than 80 K (He et al. 2016a). Although there has been no direct measurement of the sticking coefficient of CO onto p-ASW, this may also be unity because the sticking coefficient of N₂ onto p-ASW is unity at temperatures below 26.5 K (Kimmel et al. 2001) and because the sticking coefficient of CO onto np-ASW is unity at temperatures lower than 50 K (He et al. 2016a). The behavior of Equation (2) appears as a straight line with a negative slope of $-E_{sd}/2R$ on

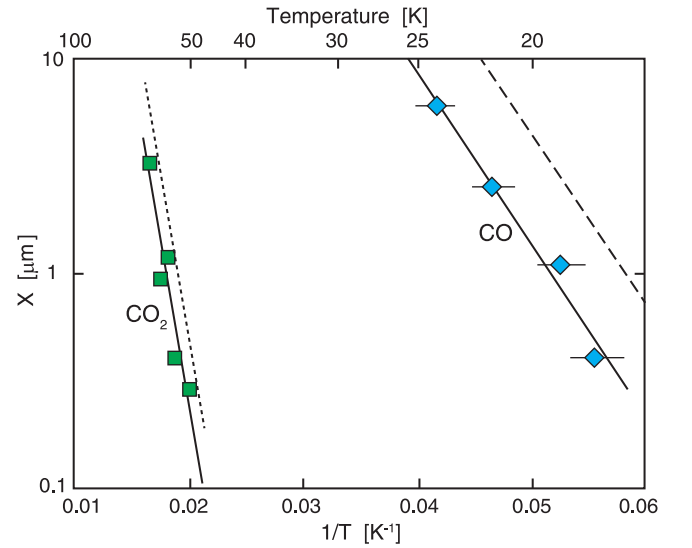


Figure 4. Plot of mean diffusion distance vs. inverse of temperature. From the saturated number densities of crystals in Figure 3, mean diffusion distances are calculated.

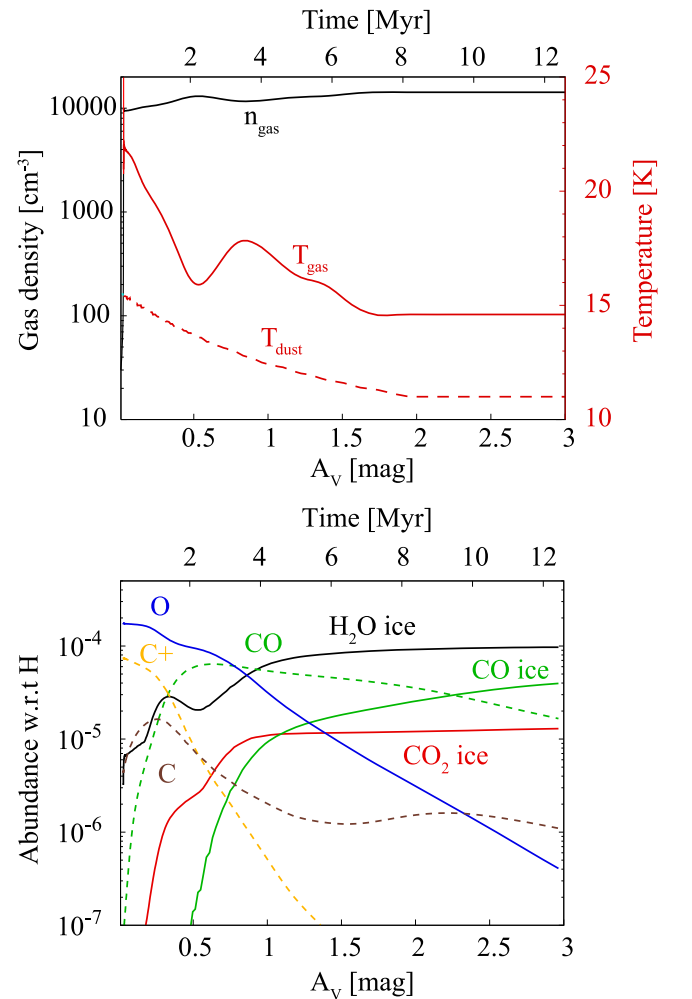


Figure 5. Top panel: physical evolution of the molecular cloud as a function of visual extinction, or time. Bottom panel: fractional abundances of selected species with respect to hydrogen nuclei as function of visual extinction or time. The solid lines represent icy species (surface + mantle), whereas the dashed lines represent gaseous species.

the plot of $\ln X$ versus $1/T$ in Figure 4. We obtained an E_{sd} of CO ($E_{\text{sd}}(\text{CO})$) on p-ASW and E_{sd} of CO₂ ($E_{\text{sd}}(\text{CO}_2)$) on np-ASW of 350 ± 50 and 1500 ± 100 K, respectively. He et al. (2016b) measured the surface coverage dependence of the binding energy of CO on p-ASW. If we assume that the surface coverage of CO on p-ASW is unity, the adsorption energy of CO on p-ASW would be 1028 K. $E_{\text{sd}}(\text{CO})$ on p-ASW obtained in this study is 0.34 of this value. $E_{\text{sd}}(\text{CO}_2)$ on annealed ASW is 0.66 of the adsorption energies of CO₂ on np-ASW (Noble et al. 2012).

Because p-ASW is acknowledged as a very porous material with a large surface area (e.g., Stevenson et al. 1999), the surface of p-ASW is not molecularly flat but might be rough. Therefore, true diffusion distances are much larger than the projected distances obtained in the present study. If true, the plot in Figure 4 should be moved upward as shown by the broken line. Since annealed ASW at 70 K may be less porous than p-ASW, a slight correction might be needed, as shown by the dotted line. It is noted that the slopes of the plots, E_{sd} , do not change after correction. In addition, the Arrhenius plots were found to be linear throughout the temperature regions of 18–24 K for CO and 50–60 K for CO₂. These results suggest that the growth of crystalline islands is dominated by the diffusion of monomers rather than clusters because the diffusion of large clusters should be effective at high temperatures, which would cause the data to deviate from the Arrhenius plot. He et al. (2018) pointed out from the observation of dangling OH that the structure of p-ASW deposited at 10 K changes from 10 to 30 K. However, this possible structural change does not influence diffusion of CO significantly as the Arrhenius plot of CO can be reproduced by a single linear component. We, therefore, conclude that the values of E_{sd} determined in the present study are unique.

This study presents the first direct measurements of $E_{\text{sd}}(\text{CO})$ and $E_{\text{sd}}(\text{CO}_2)$ on ASW. Some previous studies have reported values of E_{sd} for CO on ASW using indirect methods such as infrared spectroscopy and temperature programmed desorption (TPD) mass spectrometry, e.g., 116 ± 174 K (Mispelaer et al. 2013), 302 ± 174 K (Karssemeijer et al. 2014), 158 ± 12 K (Lauck et al. 2015), and 490 ± 12 K (He et al. 2018). E_{sd} values have certain uncertainties when the experiments are performed at high temperatures such as 35–40 K (Mispelaer et al. 2013) or 32–50 K (Karssemeijer et al. 2014) because the desorption and diffusion of CO simultaneously occur and it is difficult to separate the two effects. Furthermore, Karssemeijer et al. (2014) reported a significantly small pre-exponential factor (D_0) of 9.2×10^{-10} (cm² s⁻¹). For reference, D_0 is roughly estimated to be 9×10^{-4} (cm² s⁻¹), assuming $D_0 = a^2\nu$, where a and ν are the typical hopping distance ($a = 0.3$ nm) and frequency factor ($\nu = 10^{12}$ s⁻¹), respectively. A minor D_0 value was also reported in Lauck et al. (2015), $D_0 = 3.1 \times 10^{-12}$ (cm² s⁻¹). These small D_0 values imply that there may be problems when calculating D_0 and E_{sd} in surface diffusion on amorphous ices using rate equation models. He et al. (2018) reported $D_0 = 10^{-6.47}$ and $E_{\text{sd}} = 490$ K and proposed that the frequency for diffusion (ν) could be several orders of magnitude smaller than that for desorption, i.e., $\nu = 1.5 \times 10^9$ s⁻¹. The difference in E_{sd} between this study (350 K) and that of He et al. (2018) can be explained by the ice preparation method, i.e., He et al. (2018) annealed ASW at 70 K for 30 minutes. As a next step, measurements of D (D_0

and E_{sd}) on various ices, such as annealed p-ASW at 70 K, compact ASW, and crystalline ices, are required to comprehend the diffusion mechanism on ices. In addition, if we can simultaneously measure the nucleation rate and growth rate of CO or CO₂ crystals, the surface energy of these crystals can be obtained as well as D (D_0 and E_{sd}).

It is important to discuss the morphologies of CO and CO₂ deposited on ASW after the surface reactions, as well as the nonthermal desorption of molecules and the sticking of icy grains. However, this study makes its focus on the E_{sd} since the morphologies of CO and CO₂ require further information on the morphologies of CO and CO₂ crystals formed by the crystallization of amorphous CO and CO₂. This will form the subject of forthcoming work. Furthermore, the method developed in this study could be applicable to infrared inactive molecules, such as N₂, O₂, and Ar.

This study demonstrates that TEM is extremely useful and promising not only for the observation of the deposition process but also for the measurement of E_{sd} . TEM images include various information concerning the texture, number, and form of grains, all of which cannot be obtained via infrared spectroscopy or TPD methods. Electron diffraction provides detailed information concerning the crystallinity, amorphous, or crystalline nature, and size of the crystals. Our UHV-TEM instrument includes an electron energy-loss spectrometer (Gatan Imaging Filter Tridium), which enables us to measure atomic compositions and to detect various functional groups. In particular, the detection of radicals (OH, O, and HO₂) is the most remarkable feature of electron energy-loss spectroscopy; such detections are nearly impossible via infrared spectroscopy or TPD. This Letter is a first report of results using UHV-TEM; other examples demonstrating the usefulness of UHV-TEM will be published in forthcoming papers.

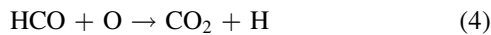
4. Efficient Formation of CO₂ in Molecular Clouds

CO₂ is one of the most abundant components of interstellar ice after H₂O; the median CO₂/H₂O abundance ratio is 26% in molecular clouds and cores (see Boogert et al. 2015 for a review). The main formation pathway of CO₂ in the interstellar medium (ISM) remains under debate. Infrared ice observations in star-forming regions indicate that the polar component of CO₂ dominates over the apolar component, suggesting that most CO₂ (approximately 80% of the overall CO₂) is embedded in H₂O within the interstellar ice (Öberg et al. 2011). The coincidence of CO₂ and H₂O ices can be naturally explained if CO₂ ice is primarily formed via the reaction



as H₂O ice is predominantly formed via OH + H → H₂O and OH + H₂ → H₂O (e.g., Garrod & Pauly 2011). In such a scenario, the formation of CO₂ ice competes with that of H₂O ice, i.e., CO diffusion competes with the hydrogenation of OH. Note that Reaction (3) in the gas phase has an activation energy barrier of 176 K (Song et al. 2006; Li et al. 2012), whereas Oba et al. (2010) found that the reaction proceeds on the ASW surface at 10 K, suggesting that the surface reaction has effectively no or very small energy barrier. Therefore, the rate-limiting step of Reaction (3) at the surface would be the diffusion of CO to OH.

Garrod & Pauly (2011) adopted the rate equation approach to investigate the formation of CO₂ ice under dark cloud conditions. They found that if $E_{\text{sd}}(\text{CO}) < 460$ K, Reaction (3) dominated CO₂ ice formation reproducing the CO₂/H₂O ice ratio observed in star-forming regions. To confirm the findings of Garrod & Pauly (2011), we re-ran the model of Furuya et al. (2015), wherein the molecular evolution in a forming and evolving molecular cloud was studied. The Furuya et al. model simulates the compression of the diffuse H I gas via supersonic accretion flows to form a denser gas (i.e., molecular clouds). Over time, the column density of the dense gas increases, shielding the interstellar UV radiation field and assisting in the accumulation of molecules. In Furuya et al. (2015), $E_{\text{sd}}(\text{CO})$ was set to 575 K and the CO₂ formation was found to be inefficient (the CO₂/H₂O ice ratio was a few percent at most). With our newly derived $E_{\text{sd}}(\text{CO})$ of 350 K, we confirmed that CO₂ ice is efficiently formed via Reaction (3), particularly at $A_V < 1$ mag, where the relatively warm dust temperature (>12 K) allows fast CO diffusion (see Figure 5). The CO₂/H₂O abundance ratio in ice reached 12% at the final time of the simulation ($A_V = 3$ mag). Conversely, Ruaud et al. (2016) claimed that



is the primary formation pathway of CO₂ ice rather than Reaction (3) under dark cloud conditions, assuming $E_{\text{sd}}(\text{CO}) = 460$ K and $E_{\text{sd}}(\text{O}) = 320$ K. Note that the laboratory experiments performed by Minissale et al. (2016) suggested a much higher $E_{\text{sd}}(\text{O})$ of 990_{-360}^{+530} K compared with the value used in Ruaud et al. (2016). In the updated Furuya et al. model, Reaction (3) does not significantly contribute to CO₂ formation. In conclusion, our newly derived CO diffusion activation energy of 350 K and the astrochemical model support a scenario wherein CO₂ ice is primarily formed via Reaction (3) in the ISM.

The authors thank two anonymous reviewers for constructive comments. This work was supported by the Ministry of Education, Culture, Sports, Science, and Technology Grants-in-Aid for Scientific Research (KAKENHI; grant JP25108002) and Japan Society for the Promotion of Science Grants-in-Aid for Scientific Research (KAKENHI; grants JP16H04072, JP17H06087).

ORCID iDs

Kenji Furuya  <https://orcid.org/0000-0002-2026-8157>
 Tetsuya Hama  <https://orcid.org/0000-0002-4991-4044>
 Takashi Kozasa  <https://orcid.org/0000-0003-0351-1968>
 Naoki Watanabe  <https://orcid.org/0000-0001-8408-2872>

References

- Boogert, A., Gerakines, P., & Whittet, D. 2015, *ARA&A*, **53**, 541
 Collings, M. P., Denver, J. W., Fraser, H. J., & McCoustra, M. R. S. 2003, *Ap&SS*, **285**, 633
 Furuya, K., Aikawa, Y., Hincelin, U., et al. 2015, *A&A*, **584**, A124
 Garrod, R. T., & Pauly, T. 2011, *ApJ*, **735**, 15
 Hama, T., & Watanabe, N. 2013, *ChRv*, **113**, 8783
 He, J., Acharyya, K., & Vidali, G. 2016a, *ApJ*, **823**, 56
 He, J., Acharyya, K., & Vidali, G. 2016b, *ApJ*, **825**, 89
 He, J., Emtiaz, M., & Vidali, G. 2017, *ApJ*, **837**, 65
 He, J., Emtiaz, S. M., & Vidali, G. 2018, *ApJ*, **863**, 156
 Heide, H.-G. 1984, *Ultramicroscopy*, **14**, 271
 Hirth, J. P., & Pound, G. M. 1963, *Condensation and Evaporation* (Oxford: Pergamon)
 Honjo, G., Kitamura, N., Shimaoka, K., & Maihara, K. 1956, *JPSJ*, **11**, 527
 Iqbal, W., Wakelam, V., & Gratier, P. 2018, *A&A*, **620**, A109
 Jenniskens, P., & Blake, D. F. 1994, *Sci*, **265**, 753
 Jenniskens, P., & Blake, D. F. 1996, *ApJ*, **473**, 1101
 Karssemeijer, L. J., Ioppolo, S., van Hemert, M. C., et al. 2014, *ApJ*, **781**, 16
 Kimmel, G. A., Stevenson, K. P., Dohnálek, Z., Smith, R. S., & Kay, B. D. 2001, *JChPh*, **114**, 5284
 Kouchi, A. 1990, *JCrGr*, **99**, 1220
 Kouchi, A., Hama, T., Kimura, Y., et al. 2016, *CPL*, **658**, 287
 Kouchi, A., Yamamoto, T., Kozasa, T., Kuroda, T., & Greenberg, J. M. 1994, *A&A*, **290**, 1009
 Lauck, T., Karssemeijer, L., Ahlenberger, K., et al. 2015, *ApJ*, **801**, 118
 Li, J., Xie, C., Ma, J., et al. 2012, *JPCA*, **116**, 5057
 Minissale, M., Congiu, E., & Dulieu, F. 2016, *A&A*, **585**, A146
 Mispelaer, F., Theulé, P., Aouididi, H., et al. 2013, *A&A*, **555**, A13
 Noble, J. A., Congiu, E., Dulieu, F., & Fraser, H. J. 2012, *MNRAS*, **421**, 768
 Oba, Y., Watanabe, N., Kouchi, A., Hama, T., & Pirronello, V. 2010, *ApJL*, **712**, L174
 Öberg, K. I., Boogert, A. C. A., Pontoppidan, K. M., et al. 2011, *ApJ*, **740**, 109
 Öberg, K. I., Fayolle, E. C., Cuppen, H. M., van Dishoeck, E. F., & Linnartz, H. 2009, *A&A*, **505**, 183
 Ruaud, M., Wakelam, V., & Hersant, F. 2016, *MNRAS*, **459**, 3756
 Smith, D. L. 1995, *Thin-Film Deposition: Principles and Practice* (Boston: McGraw-Hill)
 Song, X., Li, J., Hou, H., & Wang, B. 2006, *JChPh*, **125**, 094301
 Stevenson, K. P., Kimmel, G. A., Dohnálek, Z., Smith, R. S., & Kay, B. D. 1999, *Sci*, **283**, 1505
 Tachibana, S., Kouchi, A., Hama, T., et al. 2017, *SciA*, **3**, eaao2538
 Vertsner, V. N., & Zhdanov, G. L. 1966, *Sov. Phys. Cryst.*, **10**, 597
 Watanabe, N., & Kouchi, A. 2002, *ApJL*, **571**, L173
 Watanabe, N., & Kouchi, A. 2008, *PrSS*, **83**, 439